

Stimulated Raman Spectroscopy with Entangled Light: Enhanced Resolution and Pathway Selection

Konstantin E. Dorfman,^{*,†} Frank Schlawin,^{†,‡} and Shaul Mukamel[†]

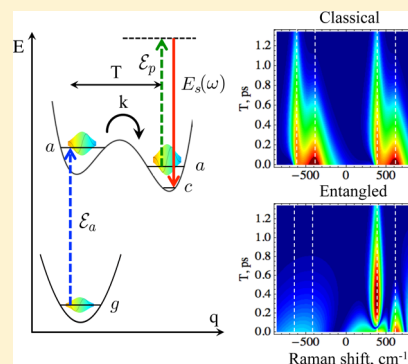
[†]Department of Chemistry, University of California, Irvine, California 92697-2025, United States

[‡]Physikalisches Institut, Albert-Ludwigs-Universität Freiburg, Hermann-Herder-Straße 3, 79104 Freiburg, Germany

S Supporting Information

ABSTRACT: We propose a novel femtosecond stimulated Raman spectroscopy (FSRS) technique that combines entangled photons with interference detection to select matter pathways and enhance the resolution. Following photoexcitation by an actinic pump, the measurement uses a pair of broad-band entangled photons; one (signal) interacts with the molecule and together with a third narrow-band pulse induces the Raman process. The other (idler) photon provides a reference for the coincidence measurement. This interferometric photon coincidence counting detection allows one to separately measure the Raman gain and loss signals, which is not possible with conventional probe transmission detection. Entangled photons further provide a unique temporal and spectral detection window that can better resolve fast excited-state dynamics compared to classical and correlated disentangled states of light.

SECTION: Spectroscopy, Photochemistry, and Excited States



Stimulated Raman spectroscopy is one of the most versatile tools for the study of molecular vibrations. Applications include probing time-resolved photophysical and photochemical processes,^{1–4} chemically specific biomedical imaging,⁵ and chemical sensing.^{6,7} Considerable effort has been devoted to eliminate the off-resonant background, thus improving the signal-to-noise ratio and the ability to detect small samples and even single molecules. Pulse shaping^{8,9} and the combination of broad- and narrow-band pulses (a technique known as femtosecond stimulated Raman spectroscopy (FSRS)¹) were employed. Recent measurements of absorption spectra with entangled photons in an interferometric setup^{10–14} suggest a possibility to use more elaborate detection. Here, we propose an interferometric FSRS (IFSRS) technique that combines quantum entangled light with interferometric detection to significantly enhance the resolution and selectivity of Raman signals. By counting photons, IFSRS can further measure separately the gain and loss contributions to the Raman spectra,¹⁵ which is not possible with classical FSRS.

Entangled light is widely used in quantum information,^{16,17} secure communication,¹⁸ and quantum computing¹⁹ applications. It has been demonstrated that the twin photon state may be used to manipulate two-photon absorption $\omega_1 + \omega_2$ type resonances in aggregates,^{20–23} but these ideas do not apply to Raman $\omega_1 - \omega_2$ resonances. We show that this can be achieved by using interferometric photon coincidence detection, which further enhances the signal-to-noise ratio. Moreover, entangled two-photon absorption has also been shown experimentally to scale linearly rather than quadratically with the pump intensity,^{21,24} thus allowing one to use

very weak light intensities, limiting damage and overcoming the photodetector noise when employing the photon coincidence measurement.²⁵

In conventional FSRS, an actinic resonant pulse \mathcal{E}_a first creates a vibrational wave packet in an electronically excited state (see Figure 1a,b). After a delay T , the frequency-resolved transmission of a broad-band (femtosecond) probe \mathcal{E}_s in the presence of a narrow-band (picosecond) pump \mathcal{E}_p shows excited-state vibrational resonances generated by an off-resonant stimulated Raman process. The FSRS signal is given by²⁶

$$S_{\text{FSRS}}(\omega, T) = \frac{2}{\hbar} I \int_{-\infty}^{\infty} dt e^{i\omega(t-T)} \mathcal{E}_s^*(\omega) \mathcal{E}_p(t) \times \langle \mathcal{T} \alpha(t) e^{-(i/\hbar) \int H_-(\tau) d\tau} \rangle \quad (1)$$

where α is the electronic polarizability, I denotes the imaginary part, $\langle \dots \rangle = \text{tr}[\dots \rho]$, with ρ being the density operator of the entire system, and $\mathcal{E}_s = \langle \mathcal{E}_s \rangle$ is the expectation value of the probe field operator with respect to the classical state of light (hereafter, \mathcal{E} denotes classical fields and E stands for quantum fields). H_- is the Hamiltonian superoperator²⁷ in the interaction picture (see section S1 of the Supporting Information (SI)), and \mathcal{T} denotes superoperator time ordering. The exponent in eq 1 can be expanded perturbatively in field–matter interactions (see section S2 of

Received: June 3, 2014

Accepted: July 11, 2014

Published: July 11, 2014

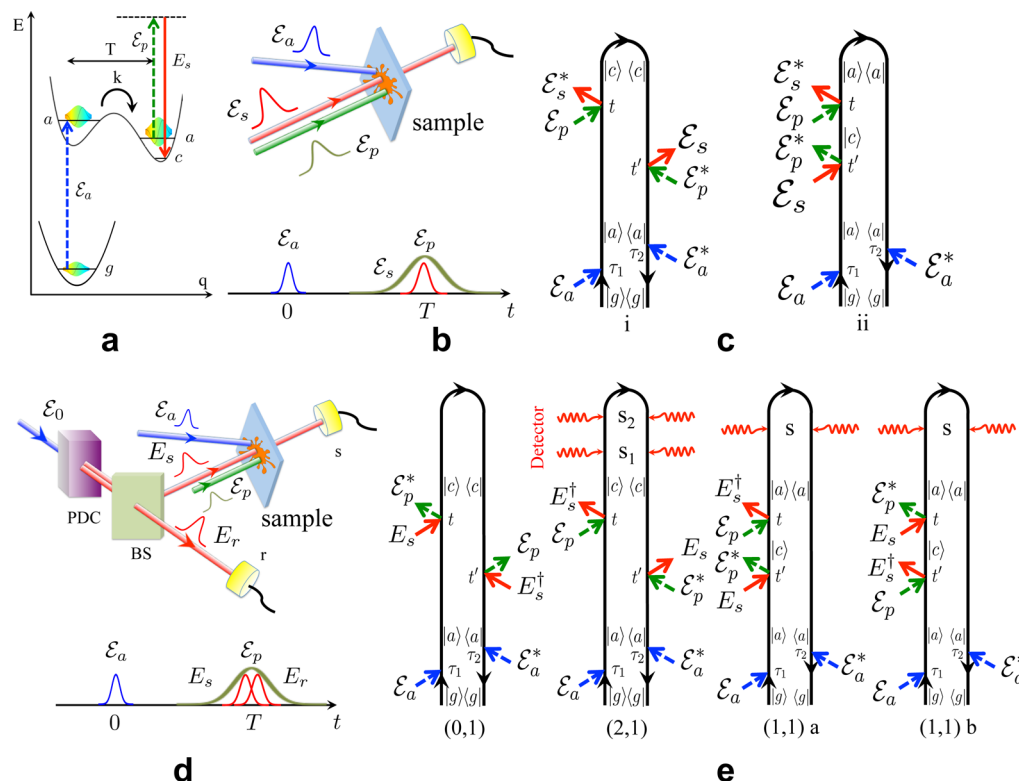


Figure 1. (Top row) Classical FSRS level scheme for the tunneling model (a), pulse configuration (b), and loop diagrams (for diagram rules, see ref 37) for classical FSRS (c). (d,e) The same as (b) and (c) but for IFSRS. The pairs of indices (0,1) and so forth in (e) indicate the number of photons registered by detectors s and r in each photon counting signal, (N_s, N_r) .

the SI). Off-resonance Raman processes can be described by the radiation–matter interaction Hamiltonian $H'(t) = \alpha E_s^\dagger(t) \mathcal{E}_p(t) + \mathcal{E}_a^*(t) V + \text{H.c.}$, where V is the dipole moment and α is the off-resonant polarizability. In the present applications, we expand the signal (eq 1) to sixth order in the fields $\sim \mathcal{E}_s^2 \mathcal{E}_p^2 \mathcal{E}_a^2$. The resulting classical FSRS signal is given by the two diagrams in Figure 1c, which translates into eqs S5 and S6 of the SI. All relevant matter information is contained in the two four-point correlation functions

$$F_i(t_1, t_2, t_3) = \langle V G^\dagger(t_1) \alpha G^\dagger(t_2) \alpha G(t_3) V^\dagger \rangle \quad (2)$$

$$F_{ii}(t_1, t_2, t_3) = \langle V G^\dagger(t_1) \alpha G(t_2) \alpha G(t_3) V^\dagger \rangle \quad (3)$$

where the retarded Green's function $G(t) = (-i/\hbar)\theta(t)e^{-iHt}$ represents forward time evolution with the free-molecule Hamiltonian and G^\dagger represents backward evolution. F_i involves one forward and two backward evolution periods, while F_{ii} contains two forward followed by one backward propagation. F_i and F_{ii} differ by the final state of the matter. In F_i (F_{ii}), it is different (the same) from the state prepared by the actinic pulse.

To use entangled light in the IFSRS measurement, we first generate frequency and polarization entangled photon pairs via type-II parametric down conversion (PDC).²⁸ The barium borate (BBO) crystal pumped by a femtosecond pulse creates a pair of orthogonally polarized photons that are initially separated by a polarizing beam splitter (BS) in Figure 1d and then directed into two arms of the Hanbury–Brown–Twiss interferometer.²⁹ Horizontally polarized beam s interacts with the molecule and serves as a Raman probe in a standard FSRS setup, whereas vertically polarized beam r propagates freely

and provides a reference. The time- and frequency-resolved detection via ultrafast upconversion of the photons³⁰ in IFSRS provides spectroscopic information about excited-state vibrational dynamics of the molecule in the s arm. IFSRS has the following control knobs: the time and frequency parameters of the single-photon detectors, which can time the photons with up to ~ 100 fs resolution,³⁰ frequency of the narrow-band classical pump pulse ω_p and, the time delay T between the actinic pulse \mathcal{E}_a and the probe \mathcal{E}_s .

The photon state produced by PDC has two contributions, a vacuum state and two-photon state with a single photon in the s mode and single photon in the r mode. It is described by the wave function

$$|\psi\rangle = |0\rangle + \int_{-\infty}^{\infty} d\omega_s d\omega_r \Phi(\omega_s, \omega_r) a_{\omega_s}^\dagger a_{\omega_r}^\dagger |0\rangle \quad (4)$$

where $a_{\omega_s}^\dagger$ ($a_{\omega_r}^\dagger$) is the creation operator of a horizontally (vertically) polarized photon and the two-photon amplitude $\Phi(\omega_s, \omega_r)$ is given by²²

$$\Phi(\omega_s, \omega_r) = \mathcal{E}_0(\omega_s + \omega_r) \sum_{i \neq j=1}^2 \text{sinc}\left(\frac{\omega_{s0} T_i}{2} + \frac{\omega_{r0} T_j}{2}\right) \times e^{(i\omega_{s0} T_i/2) + (i\omega_{r0} T_j/2)} \quad (5)$$

where $\omega_{k0} = \omega_k - \omega_0$, $k = s, r$ is the frequency difference between the entangled photon and the classical PDC-pump field \mathcal{E}_0 that created an entangled pair. In the following simulations, we assumed a Lorentzian field envelope $\mathcal{E}_0(\omega) = A_0/[\omega - \omega_0 + i\sigma_0]$. $T_j = [(1/\nu_p) - (1/\nu_i)]L$, $k = s, r$ is the time delay acquired by the entangled photon relative to the PDC-pump field due to group velocity dispersion

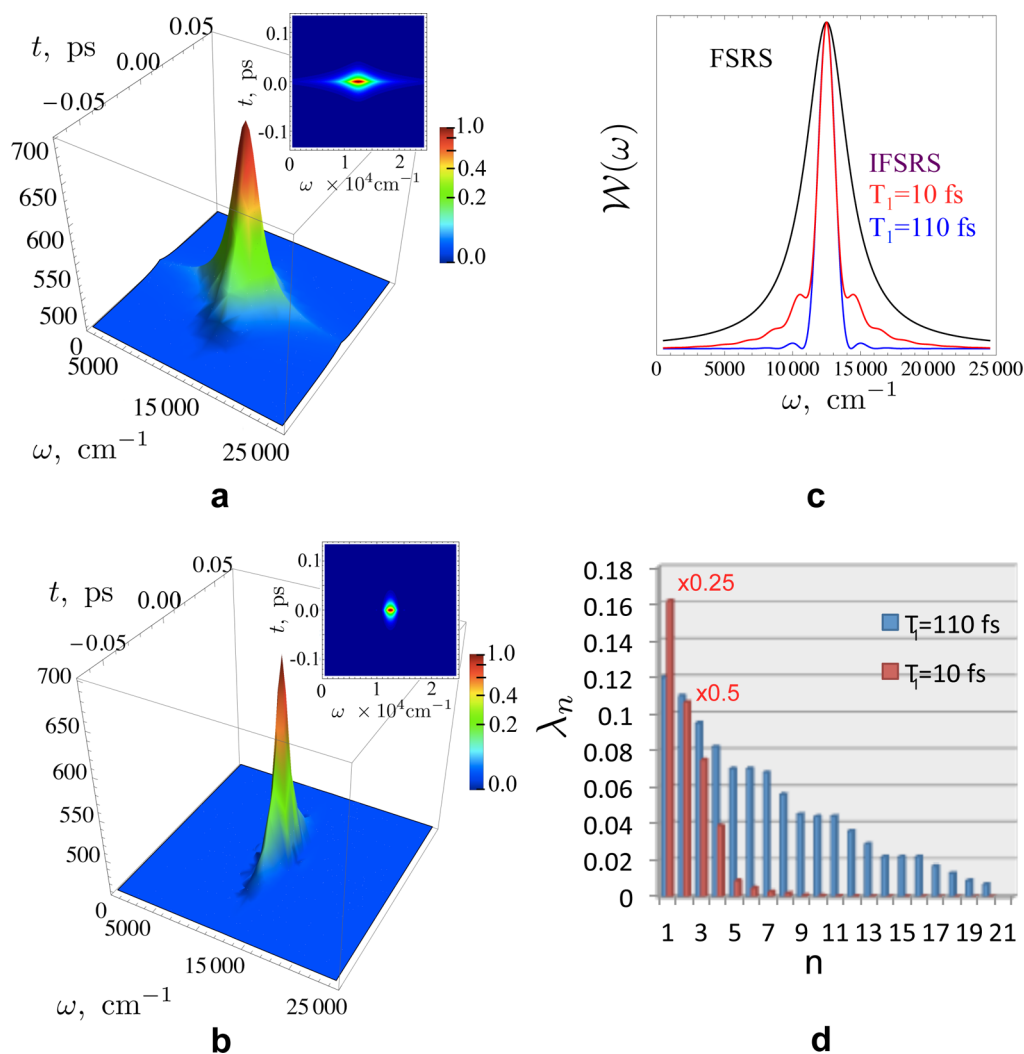


Figure 2. (Left column) (a) Time–frequency Wigner spectrogram for classical light, (b) same as (a) but for the entangled twin state given by eq 4. The insets depict a 2D prejection. (Right column) (c) Window function $\mathcal{W}(\omega)$ for FSRs $\mathcal{E}_s^*(\omega)\mathcal{E}_s(\omega + i\gamma_a)$ (black) and IFSRS $\Phi^*(\omega, \bar{\omega}_r)\Phi(\omega + i\gamma_a, \bar{\omega}_r)$, with $T_1 = 110 \text{ fs}$ (blue), $T_2 = 120 \text{ fs}$ and $T_1 = 10 \text{ fs}$, $T_2 = 120 \text{ fs}$ (red). (d) Spectrum of the eigenvalues λ_n in the Schmidt decomposition (eq 6) for the entangled state with the amplitude (eq 5). The first two eigenvalues $n = 1$ and 2 are scaled with weights 0.25 and 0.5 , respectively. The remaining eigenvalues have no weighted scaling.

inside the nonlinear crystal. $T_{12} = T_2 - T_1$ is the entanglement time, which controls the timing of the entangled pair. For a narrow-band PDC-pump $\mathcal{E}_0(\omega)$, the sum-frequency $\omega_s + \omega_r$ is narrowly distributed around $2\omega_0$ with bandwidth σ_0 . This has been used to selectively prepare double exciton states in two-photon absorption.^{21,22} For a broad-band PDC-pump, the frequency difference $\omega_s - \omega_0$ is narrow with bandwidth T_j^{-1} , $j = 1, 2$.²³ The output state of light in mode s may contain a varying number of photons, depending on the order of the field–matter interaction.

In general, the twin photon state eq 4 is not necessarily entangled. This can be determined by the Schmidt decomposition³¹

$$\Phi(\omega_s, \omega_r) = \sum_n \sqrt{\lambda_n} \psi_n(\omega_s) \phi_n(\omega_r) \quad (6)$$

where λ_k are the real positive singular values of Φ and $\psi_n(\phi_n)$ form an orthonormal set of eigenfunctions of $\int d\omega \Phi(\omega_s, \omega) \Phi^*(\omega_r, \omega)$ ($\int d\omega \Phi(\omega, \omega_s) \Phi^*(\omega, \omega_r)$), with $\sum_n \lambda_n = 1$ for the normalized two-photon state. A separable

(unentangled) state has only one nonvanishing eigenvalue $\lambda_1 = 1$, whereas two or more components imply entanglement. The degree of entanglement can be measured by the inverse participation ratio $r_p \equiv (\sum_n \lambda_n^2)^{-1}$. For the two-photon amplitude in eq 5, the rich spectrum of eigenvalues shown in Figure 2d indicates that the state is highly entangled as $r_p \approx 100$. In addition, as can be seen from the inset in Figure 2a,b, the state (eq 5) is not bound by the Fourier uncertainty $\Delta\omega\Delta t \geq 1$. In the following, we study effects of the entanglement on Raman resonances.

The IFSRS is given by the rate of a joint time- and frequency-gated detection of N_s photons in detector s and a single photon in r when both detectors have narrow spectral gating. This is given by

$$S_{\text{IFSRS}}^{(N_s, 1)}(\bar{\omega}_{s_1}, \dots, \bar{\omega}_{s_{N_s}}, \bar{\omega}_r, \Gamma_i) = \langle \mathcal{T} E_r^\dagger(\bar{\omega}_r) E_r(\bar{\omega}_r) \prod_{j=1}^{N_s} E_s^\dagger(\bar{\omega}_{s_j}) E_s(\bar{\omega}_{s_j}) e^{-(i/\hbar) \int_{-\infty}^{\infty} H'_-(\tau) d\tau} \rangle \quad (7)$$

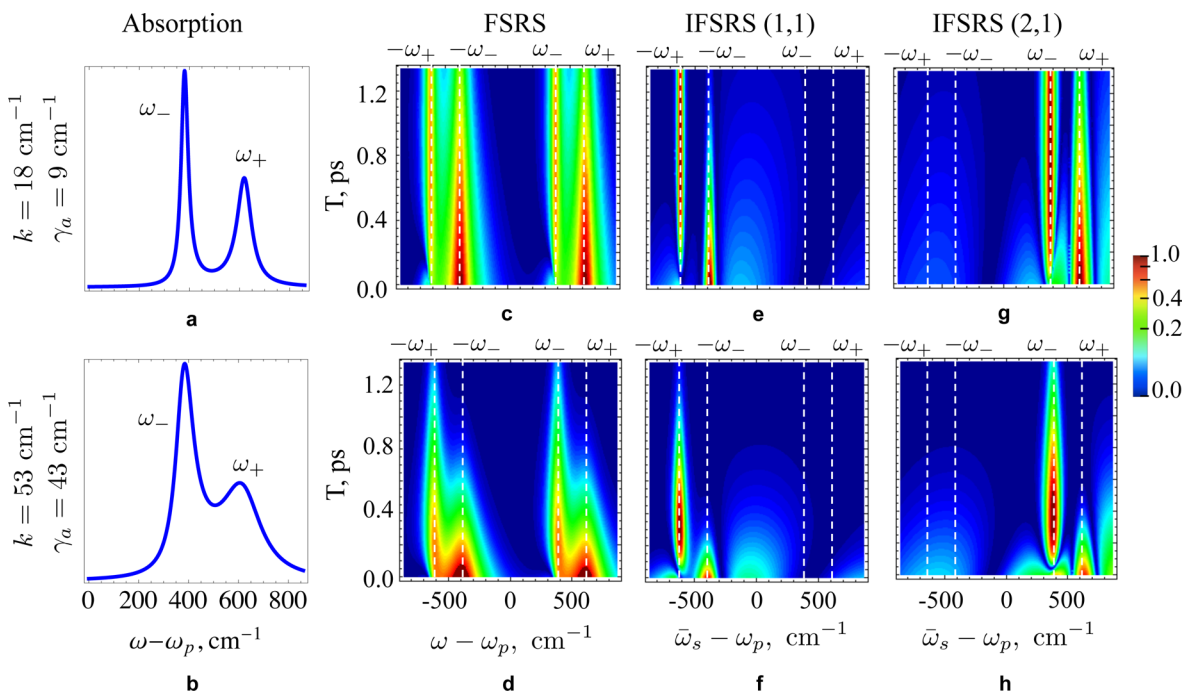


Figure 3. (First column) (a) Absorption for a time-evolving vibrational mode versus $\omega - \omega_p$ for slow tunneling rate $k = 18 \text{ cm}^{-1}$ and narrow dephasing $\gamma_a = 9 \text{ cm}^{-1}$; (b) same as (a) but for fast tunneling rate $k = 53 \text{ cm}^{-1}$ and broad dephasing $\gamma_a = 43 \text{ cm}^{-1}$. (Second column) (c,d) Same as (a,b) but for a classical FSR signal. (Third column) (e,f) Same as (a,b) but for $S_{\text{IFSRS}}^{(1,1)}$. (Fourth column) (g,h) Same as (a,b) but for $S_{\text{IFSRS}}^{(2,1)}$ given by eq 9 versus $\bar{\omega}_s - \omega_p$. Parameters for the simulations: unperturbed vibrational frequency $\omega_{ac} = 500 \text{ cm}^{-1}$, level splitting $\delta = 120 \text{ cm}^{-1}$, $\omega_p = 12500 \text{ cm}^{-1}$, $\bar{\omega}_r = 15500 \text{ cm}^{-1}$, and $T_2 = 120 \text{ fs}$. $T_1 = 10 \text{ fs}$ for (c,d), and $T_1 = 110 \text{ fs}$ for (e,f). The series of snapshots (slices of panels c–h) are shown in Figure S1 of the SI.

where Γ_i represents the incoming light beams, such as the central frequency and time and spectral and temporal bandwidth. In the standard Glauber's approach,³² photon counting is calculated in the space of the radiation field using normally ordered field operators. Equation 7 in contrast operates in the joint matter plus field space and uses time-ordered superoperators.³³ This is necessary for the book-keeping of spectroscopic signals. Both FSR and IFSRS signals are obtained by the lowest (sixth-) order perturbative expansion of eq 7 in field–matter interactions (section S2 of the SI), as depicted by the loop diagrams shown in Figure 1c and e, respectively. Measurements with a different number of photons in the s arm are experimentally distinct and are given by different detection windows governed by the multipoint correlation function of the electric field (red arrows in Figure 1e). Details of the derivations for the field correlation functions for the twin entangled state of light are given in section S3 of the SI.

Figure 2 compares field spectrograms that represent the windows created by various fields. Figure 2a depicts a time–frequency Wigner function $W_s(\omega, t) = \int_{-\infty}^{\infty} (d\Delta / 2\pi) \mathcal{E}_s^*(\omega) \mathcal{E}_s(\omega + \Delta) e^{-i\Delta t}$ for the classical probe field \mathcal{E}_s . The time–frequency Fourier uncertainty restricts the frequency resolution for a given time resolution so that $\Delta\omega\Delta t \geq 1$. The Wigner spectrogram $W_q(\omega, t; \bar{\omega}_r) = \int_{-\infty}^{\infty} (d\Delta / 2\pi) \Phi^*(\omega, \bar{\omega}_r) \Phi(\omega + \Delta, \bar{\omega}_r) e^{-i\Delta t}$ for the entangled twin photon state is depicted in Figure 2b. For the same temporal resolution as that in FSR ($\Delta\nu\Delta t \approx 3.7 \text{ ps}\cdot\text{cm}^{-1}$, which is the Fourier uncertainty for the classical Lorentzian pulses), the spectral resolution of IFSRS is significantly better ($\Delta\nu\Delta t \approx 1.6 \text{ ps}\cdot\text{cm}^{-1}$). This is possible because the time and frequency resolution for entangled light are not Fourier conjugate

variables.²² The high spectral resolution in the entangled case is governed by T_j^{-1} , $j = 1, 2$, which is narrower than the broad-band probe pulse. Figure 2c demonstrates that the entangled window function $R_q^{(N_s, 1)}$ for $N_s = 1, 2$ (see eqs S35 and S31, SI) that enters the IFSRS (eq 9) yields a much higher spectral resolution than the classical R_c in eq S25 (SI).

The molecular information required by the Raman measurements considered here is given by two correlation functions F_i and F_{ii} (see Figure 1c,e and eqs 2 and 3). These are convoluted with a different detection window for FSR and IFSRS. F_i and F_{ii} may not be separately detected in FSR. However, in IFSRS, the loss $S_{\text{IFSRS}}^{(0,1)}$ and the gain $S_{\text{IFSRS}}^{(2,1)}$ Raman signals probe F_{ii} , where the final state c can be different from initial state a . On the other hand the coincidence counting $S_{\text{IFSRS}}^{(1,1)}$ signal is related to F_{ii} (both initial and final states are the same a). Interferometric signals can thus separately detect F_i and F_{ii} .

IFSRS for a Vibrational Mode in a Tunneling System. We demonstrated the combined effect of entanglement and interferometric measurement by calculating the signals for the three-level model system undergoing relaxation, as depicted in Figure 1a. Once excited by the optical pulse, the vibrational state of the excited electronic state at the initial time has frequency $\omega_{a+} = \omega_a + \delta$. For a longer time, the system tunnels through a barrier at a rate k and assumes a different frequency $\omega_{a-} = \omega_a - \delta$. The probability to be in the state with ω_{a+} decreases exponentially as $P_+(t) = e^{-kt}$, whereas for ω_{a-} , it grows as $P_-(t) = 1 - e^{-kt}$. This model is mathematically identical to the low-temperature limit of Kubo's two-state jump model described by the stochastic Liouville equation (SLE).^{34,35} The absorption line shape is given by

$$S_1(\omega) = -I \frac{4}{\hbar^2} |\mathcal{E}(\omega)|^2 \frac{|\mu_{ag}|^2}{k + 2i\delta} \times \left(\frac{k + i\delta}{\omega - \omega_{a-} + i\gamma_a} + \frac{i\delta}{\omega - \omega_{a+} + i(\gamma_a + k)} \right) \quad (8)$$

This gives two peaks with combined width governed by dephasing γ_a and tunneling rate k . Similarly, one can derive the corresponding IFSRS signal $S_{\text{IFSRS}}^{(N_s,1)}$ with $N_s = 0-2$ using SLE (see section S4 of the SI), which yields

$$S_{\text{IFSRS}}^{(N_s,1)}(\bar{\omega}_s, \bar{\omega}_r; \omega_p, T) = I \frac{\mu}{\hbar^4} |\mathcal{E}_p|^2 |\mathcal{E}_a|^2 \sum_{a,c} \alpha_{ac}^2 |\mu_{ag}|^2 \times e^{-2\gamma_a T} \left(R_q^{(N_s,1)}(\bar{\omega}_s, \bar{\omega}_r, 2\gamma_a, \bar{\nu}\omega_\nu - i\gamma_a) - \frac{2i\delta e^{-kT}}{k + 2i\delta} \times [R_q^{(N_s,1)}(\bar{\omega}_s, \bar{\omega}_r, 2\gamma_a + k, \bar{\nu}\omega_\nu - i\gamma_a) - R_q^{(N_s,1)}(\bar{\omega}_s, \bar{\omega}_r, 2\gamma_a + k, \bar{\nu}\omega_\nu - i(\gamma_a + k))] \right) \quad (9)$$

where $\nu = -$ for $N_s = 0, 2$ and $\nu = +$ for $N_s = 1$ and $\mu = -$ for $N_s = 1, 2$ and $\mu = +$ for $N_s = 0$, $\omega_\pm = \omega_{a\pm} - \omega_c$. Expressions for the Raman response $R_q^{(N_s,1)}$, which depends on the window created by the quantum field for different photon numbers N_s , are given by eqs S27, S31, and S35 of the SI. The classical FSRS signal (eq 1) is given by the similar expression, that is, $S_{\text{FSRS}}^{(c)} = S_{\text{IFSRS}}^{(2,1)}[\omega_\pm] - S_{\text{IFSRS}}^{(2,1)}[-\omega_\mp]$ by replacing the entangled detection window $\Phi^*(\omega, \bar{\omega}_r)\Phi(\omega + i\gamma, \bar{\omega}_r)$ with a classical one $\mathcal{E}_s^*(\omega)\mathcal{E}_s(\omega + i\gamma)$.

Figure 3 compares the classical FSRS signal (eq S24, SI) with $S_{\text{IFSRS}}^{(1,1)}$ and $S_{\text{IFSRS}}^{(2,1)}$ (eq 9). For slow modulation and a long dephasing time $k\gamma_a \ll \delta$, the absorption (Figure 3a) has two well-resolved peaks at ω_\pm . The classical FSRS shown in Figure 3c then has one dominant resonance at ω_+ , which decays with the delay T , whereas the ω_- peak slowly builds up and dominates at longer T . This signal contains both blue- and red-shifted Raman resonances relative to the narrow-band pump frequency, $\omega - \omega_p = \pm\omega_\pm$. If the modulation and dephasing rates are comparable to the level splitting $k\gamma_a \approx \delta$, then the ω_\pm resonances in the absorption (Figure 3b) and the classical FSRS (Figure 3d) become broad and less resolved. It is worth noting, that there is no mirror symmetry between blue and red contributions around $\omega = \omega_p$. For $\omega > \omega_p$, the vibration probed by a Raman sequence of pulses at initial time has frequency $\omega - \omega_p = \omega_+ = \omega_{ac} + \delta$, which gets depopulated with time, whereas the transition $\omega - \omega_p = \omega_- = \omega_{ac} - \delta$ gets populated. In the case of $\omega < \omega_p$, the higher vibrational state is given by $-\omega_-$, and the lower vibrational state is $-\omega_+$. Therefore, the actual symmetry applies to $\omega_\pm \leftrightarrow -\omega_\mp$.

We next turn to IFSRS. For slow tunneling and long dephasing, $S_{\text{IFSRS}}^{(1,1)}$ is similar to the classical FSRS as shown in Figure 3e. However, both temporal and spectral resolutions remain high even when the modulation is fast and the dephasing width is large, as is seen in Figure 3f. The same applies to the $S_{\text{IFSRS}}^{(2,1)}$ signal depicted for slow tunneling (Figure 3g) and fast tunneling (Figure 3h). Note that high resolution for the $S_{\text{IFSRS}}^{(1,1)}$ and $S_{\text{IFSRS}}^{(2,1)}$ signals is achieved for different parameter regimes. At fixed $T_2 = 120$ fs, $S_{\text{IFSRS}}^{(1,1)}$ has high

resolution at short $T_1 = 10$ fs, whereas long $T_1 = 110$ fs works better for $S_{\text{IFSRS}}^{(2,1)}$. This difference may be attributed to the selection of field-matter pathways by the different detection windows of the two signals. Another important difference between the long and short dephasing (top and bottom rows in Figure 3, respectively) is the overall time scale. It follows from eqs S24 (SI) and 9 that the signals decay exponentially with the dephasing rate $\approx e^{-2\gamma_a T}$. Therefore, for a given range of $0 < T < 1.3$ ps, the signals with long dephasing (panels c, e, and g in Figure 3) are stronger than the signals with fast dephasing (panels d, f, and g in Figure 3).

Apart from the different detection windows, there is another important distinction between IFSRS (eq 9) and FSRS (eq S24, SI) signals. In FSRS, the gain and loss contributions both contain red- and blue-shifted features relative to the narrow pump. The FSRS signal can contain both Stokes and anti-Stokes components. Classical FSRS can only distinguish between red and blue contributions. The counting signals, in contrast, can measure separately the gain $S_{\text{IFSRS}}^{(2,1)}$ and the loss $S_{\text{IFSRS}}^{(0,1)}$ contributions because these are not related to the classical causal response function, which is a specific combination of the quantum matter pathways. Each IFSRS signal is a different combination of pathways that can be expressed uniquely in terms of the left and right superoperators.

Role of Entanglement. We now show that entanglement is essential for the improved resolution of Raman resonances, which may not be achieved by classically shaped light. To that end, we calculate the IFSRS signals (eq 9) for the correlated-separable state of the field³⁶ described by the density matrix $\rho_{\text{cor}} = \int_{-\infty}^{\infty} d\omega_s d\omega_r |\Phi(\omega_s, \omega_r)\rangle \langle 1_{\omega_s} 1_{\omega_r}|$. This is the diagonal part of the density matrix corresponding to the state (eq 4) with amplitude (eq 5). This state is not entangled but yields the same single-photon spectrum and shows strong frequency correlations similar to the entangled case and is typically used as a benchmark to quantify entanglement in quantum information processing.³¹ We further examine the fully separable uncorrelated Fock state given by eq 4 with $\Phi_{\text{uncor}}(\omega_s, \omega_r) = \Phi_s(\omega_s)\Phi_r(\omega_r)$ with $\Phi_k(\omega_k) = \Phi_0/[\omega_k - \omega_0 + i\sigma_0]$, $k = s, r$ with parameters matching the classical probe pulse used in FSRS.

$S_{\text{IFSRS}}^{(1,1)}$ for these three states of light are compared in the left column of Figure 4. Figure 4a shows highly resolved Raman resonances for the entangled twin state. The separable correlated state (see Figure 4b) has high spectral but no temporal resolution, as expected from a continuous-wave time-averaged state in which the photons arrive at any time.³⁶ The separable uncorrelated state (see Figure 4c) yields the same resolution as the classical FSRS signal in Figure 3d because the correlation function of the field factorizes into a product of field amplitudes. Similar results can be obtained for the $S_{\text{IFSRS}}^{(2,1)}$ (see Figure 4d–f). Derivations of the IFSRS signals for the correlated and uncorrelated separable states are given in section S5 of the SI.

In summary, we have demonstrated that stimulated Raman signals with quantum field and interferometric detection better reveal detailed molecular information that is not possible by the standard heterodyne detection of classical fields.

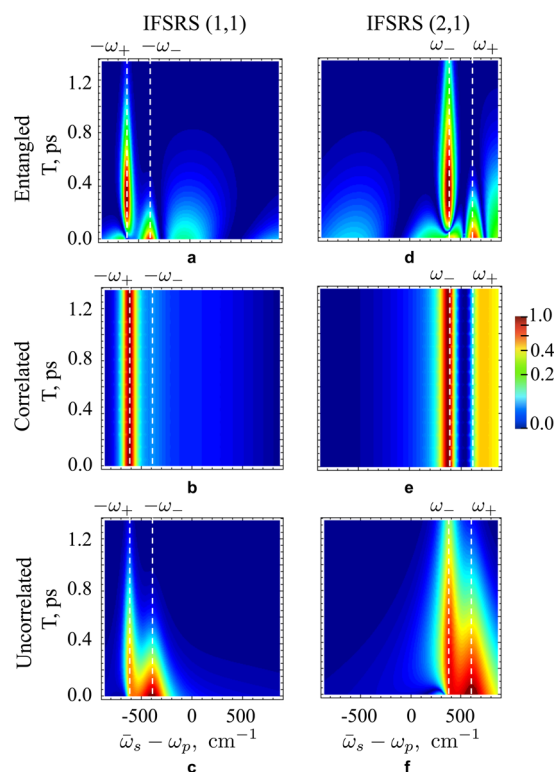


Figure 4. (Left column) $S_{\text{IFSRS}}^{(1,1)}$ signal versus $\bar{\omega}_s - \omega_p$ for the entangled state (eq 5) (a) and correlated (b) and uncorrelated (c) separable states. (d–f) Same as (a–c) but for the $S_{\text{IFSRS}}^{(2,1)}$ signal. All parameters are the same as those in Figure 3. The corresponding series of snapshots (slices of these plots) are shown in Figure S2 of the SI.

THEORETICAL METHODS

In order to use quantum light as a spectroscopic tool for studying complex models of matter, the field–matter interactions must be described in the joint field and matter space. This is done by using the superoperator loop diagram formalism.³⁷ Order by order in the field–matter interaction, the signals can be factorized into products of field and matter time-ordered superoperator correlation functions.

The leading third-order signal is governed by a four-point correlation function of the matter. Depending on the number of detected photons, this four-point matter correlation function is convoluted with different field correlation functions. For $N_s = 0$, $N_r = 1$, eq 7 is given by a four-point correlation function for a quantum field. For a twin photon state, it can be factorized as $\langle \psi | E_s^\dagger(\omega_a) | E_r^\dagger(\omega_b) E_r(\omega_c) E_s(\omega_d) | \psi \rangle = \Phi^*(\omega_a, \omega_b) \Phi(\omega_c, \omega_d)$. For $N_s = 2$, it is given by an eight-point function (see eq S8, SI), whereas for $N_s = 1$, it is governed by a six-point field correlation function, as shown in eqs S9 and S10 (SI). For the two-photon state, normally ordered field correlation functions with more than four fields vanish because extra annihilation operators act on the vacuum state. Therefore, the higher-order non-normally ordered field correlation functions can be recast as a four-point correlation function times multiple field commutators, which are given by $[E_s(\omega), E_s^\dagger(\omega')] = \mathcal{D}(\omega_p) \delta(\omega - \omega')$ where $\mathcal{D}(\omega_s) \simeq \mathcal{D}(\omega_p)$ is the constant that is assumed to be a flat function of its argument for a normalized two-photon state. Therefore, for $N_s = 2$ and 1, the signal is proportional to $\mathcal{D}^2(\omega_p)$ and

$\mathcal{D}(\omega_p)$, respectively. All three IFSRS signals with $N_s = 0$ –2 scale as $\approx |\mathcal{E}_0|^2 |\mathcal{E}_a|^2 |\mathcal{E}_p|^2$ with field intensity, the same as classical FSRS even though a different number of fields contribute to the detection.

ASSOCIATED CONTENT

Supporting Information

Details of the photon counting signals. Derivation of multiple field correlation functions for the entangled state of light. Expressions for the FSRS and IFSRS signals derived in terms of field and matter correlation functions. Corresponding FSRS and IFSRS signals for the vibrational tunneling model used in simulations along with supporting figures. Expressions for the signals for separable correlated and uncorrelated states of light. This material is available free of charge via the Internet at <http://pubs.acs.org>.

AUTHOR INFORMATION

Corresponding Author

*E-mail: kdorfman@uci.edu.

Notes

The authors declare no competing financial interest.

ACKNOWLEDGMENTS

We gratefully acknowledge the support of the National Science Foundation through Grant No. CHE-1361516, the Chemical Sciences, Geosciences and Biosciences Division, Office of Basic Energy Sciences, Office of Science, U.S. Department of Energy, and a National Institute of Health Grant No. GM-59230. DOE partially supported K.D. and the computations. F.S. would like to thank the German National Academic Foundation.

REFERENCES

- (1) Kukura, P.; McCamant, D. W.; Mathies, R. A. Femtosecond Stimulated Raman Spectroscopy. *Annu. Rev. Phys. Chem.* **2007**, *58*, 461–488.
- (2) Kukura, P.; McCamant, D. W.; Yoon, S.; Wandschneider, D. B.; Mathies, R. A. Structural Observation of the Primary Isomerization in Vision with Femtosecond-Stimulated Raman. *Science* **2005**, *310*, 1006–1009.
- (3) Takeuchi, S.; Ruhman, S.; Tsuneda, T.; Chiba, M.; Taketsugu, T.; Tahara, T. Spectroscopic Tracking of Structural Evolution in Ultrafast Stilbene Photoisomerization. *Science* **2008**, *322*, 1073–1077.
- (4) Kuramochi, H.; Takeuchi, S.; Tahara, T. Ultrafast Structural Evolution of Photoactive Yellow Protein Chromophore Revealed by Ultraviolet Resonance Femtosecond Stimulated Raman Spectroscopy. *J. Phys. Chem. Lett.* **2012**, *3*, 2025–2029.
- (5) Cheng, J.-x.; Volkmer, A.; Book, L. D.; Xie, X. S. Multiplex Coherent Anti-Stokes Raman Scattering Microspectroscopy and Study of Lipid Vesicles. *J. Phys. Chem. B* **2002**, *106*, 8493–8498.
- (6) Arora, R.; Petrov, G. I.; Yakovlev, V. V.; Scully, M. O. Detecting Anthrax in the Mail by Coherent Raman Microspectroscopy. *Proc. Natl. Acad. Sci. U.S.A.* **2012**, *109*, 1151–1153.
- (7) Bremer, M. T.; Dantus, M. Standoff Explosives Trace Detection and Imaging by Selective Stimulated Raman Scattering. *Appl. Phys. Lett.* **2013**, *103*, 061119.
- (8) Oron, D.; Dudovich, N.; Yelin, D.; Silberberg, Y. Narrow-Band Coherent Anti-Stokes Raman Signals from Broad-Band Pulses. *Phys. Rev. Lett.* **2002**, *88*, 063004.
- (9) Pestov, D.; Murawski, R. K.; Ariunbold, G. O.; Wang, X.; Zhi, M.; Sokolov, A. V.; Sautenkov, V. A.; Rostovtsev, Y. V.; Dogariu, A.; Huang, Y.; Scully, M. O. Optimizing the Laser-Pulse Configuration for Coherent Raman Spectroscopy. *Science* **2007**, *316*, 265–268.

- (10) Scarcelli, G.; Valencia, A.; Gompers, S.; Shih, Y. Remote Spectral Measurement Using Entangled Photons. *Appl. Phys. Lett.* **2003**, *83*, 5560–5562.
- (11) Yabushita, A.; Kobayashi, T. Spectroscopy by Frequency-Entangled Photon Pairs. *Phys. Rev. A* **2004**, *69*, 013806.
- (12) Kalachev, A.; Kalashnikov, D.; Kalinkin, A.; Mitrofanova, T.; Shkalikov, A.; Samartsev, V. Biphoton Spectroscopy of YAG: Er³⁺ Crystal. *Laser Phys. Lett.* **2007**, *4*, 722–725.
- (13) Slattery, O.; Ma, L.; Kuo, P.; Kim, Y.-S.; Tang, X. Frequency Correlated Biphoton Spectroscopy Using Tunable Upconversion Detector. *Laser Phys. Lett.* **2013**, *10*, 075201.
- (14) Kalashnikov, D. A.; Pan, Z.; Kuznetsov, A. I.; Krivitsky, L. A. Quantum Spectroscopy of Plasmonic Nanostructures. *Phys. Rev. X* **2014**, *4*, 011049.
- (15) Harbola, U.; Umapathy, S.; Mukamel, S. Loss and Gain Signals in Broadband Stimulated-Raman Spectra: Theoretical Analysis. *Phys. Rev. A* **2013**, *88*, 011801.
- (16) Lvovsky, A. I.; Raymer, M. G. Continuous-Variable Optical Quantum-State Tomography. *Rev. Mod. Phys.* **2009**, *81*, 299.
- (17) Lee, K. C.; et al. Entangling Macroscopic Diamonds at Room Temperature. *Science* **2011**, *334*, 1253–1256.
- (18) Gisin, N.; Ribordy, G.; Tittel, W.; Zbinden, H. Quantum Cryptography. *Rev. Mod. Phys.* **2002**, *74*, 145–195.
- (19) Kok, P.; Munro, W. J.; Nemoto, K.; Ralph, T. C.; Dowling, J. P.; Milburn, G. Linear Optical Quantum Computing with Photonic Qubits. *Rev. Mod. Phys.* **2007**, *79*, 135.
- (20) Saleh, B. E. A.; Jost, B. M.; Fei, H.-B.; Teich, M. C. Entangled-Photon Virtual-State Spectroscopy. *Phys. Rev. Lett.* **1998**, *80*, 3483–3486.
- (21) Lee, D.-I.; Goodson, T. Entangled Photon Absorption in an Organic Porphyrin Dendrimer. *J. Phys. Chem. B* **2006**, *110*, 25582–25585.
- (22) Schlawin, F.; Dorfman, K. E.; Fingerhut, B. P.; Mukamel, S. Suppression of Population Transport and Control of Exciton Distributions by Entangled Photons. *Nat. Commun.* **2013**, *4*, 1782.
- (23) Dorfman, K. E.; Mukamel, S. Multidimensional Spectroscopy with Entangled Light: Loop vs Ladder Delay Scanning Protocols. *New J. Phys.* **2014**, *16*, 033013.
- (24) Javanainen, J.; Gould, P. L. Linear Intensity Dependence of a Two-Photon Transition Rate. *Phys. Rev. A* **1990**, *41*, 5088–5091.
- (25) Penin, A. N.; Sergienko, A. V. Absolute standardless calibration of photodetectors based on quantum two-photon fields. *Appl. Opt.* **1991**, *30*, 3582.
- (26) Dorfman, K. E.; Fingerhut, B. P.; Mukamel, S. Broadband Infrared and Raman Probes of Excited-State Vibrational Molecular Dynamics: Simulation Protocols Based on Loop Diagrams. *Phys. Chem. Chem. Phys.* **2013**, *15*, 12348–12359.
- (27) Harbola, U.; Mukamel, S. Superoperator Nonequilibrium Green's Function Theory of Many-Body Systems; Applications to Charge Transfer and Transport in Open Junctions. *Phys. Rep.* **2008**, *465*, 191–222.
- (28) Shih, Y. Entangled Biphoton Source — Property and Preparation. *Rep. Prog. Phys.* **2003**, *66*, 1009.
- (29) Brown, R. H. A Test of a New Type of Stellar Interferometer on Sirius. *Nature* **1956**, *178*, 1046–1048.
- (30) Kuzucu, O.; Wong, F. N.; Kurimura, S.; Tovstionog, S. Time-Resolved Single-Photon Detection by Femtosecond Upconversion. *Opt. Lett.* **2008**, *33*, 2257–2259.
- (31) Law, C. K.; Walmsley, I. A.; Eberly, J. H. Continuous Frequency Entanglement: Effective Finite Hilbert Space and Entropy Control. *Phys. Rev. Lett.* **2000**, *84*, 5304–5307.
- (32) Glauber, R. *Quantum Theory of Optical Coherence*; Wiley: New York, 2007.
- (33) Dorfman, K. E.; Mukamel, S. Indistinguishability and Correlations of Photons Generated by Quantum Emitters Undergoing Spectral Diffusion. *Sci. Rep.* **2014**, *4*, 3996.
- (34) Kubo, R. Stochastic Liouville Equations. *J. Math. Phys.* **1963**, *4*, 174–183.
- (35) Dorfman, K. E.; Fingerhut, B. P.; Mukamel, S. Time-Resolved Broadband Raman Spectroscopies: A Unified Six-Wave-Mixing Representation. *J. Chem. Phys.* **2013**, *139*, 124113.
- (36) Zheng, Z.; Saldanha, P. L.; Rios Leite, J. R.; Fabre, C. Two-Photon–Two-Atom Excitation by Correlated Light States. *Phys. Rev. A* **2013**, *88*, 033822.
- (37) Rahav, S.; Mukamel, S. Ultrafast Nonlinear Optical Signals Viewed from the Molecules Perspective: Kramers–Heisenberg Transition Amplitudes vs. Susceptibilities. *Adv. At. Mol., Opt. Phys.* **2010**, *59*, 223.